

The X-ray corona in the black-hole binary GRO J1655–40 from the properties of non-harmonically related quasi-periodic oscillations.

Sandeep K. Rout,¹[★] Mariano Méndez,² and Federico García,³

¹*Physical Research Laboratory, Navarangpura, Ahmedabad 380009, Gujarat, India*

²*Kapteyn Astronomical Institute, University of Groningen, PO Box 800, NL-9700 AV Groningen, the Netherlands*

³*Instituto Argentino de Radioastronomía (CCT La Plata, CONICET; CICPBA; UNLP), C.C.5, (1894) Villa Elisa, Buenos Aires, Argentina*

3 August 2023

ABSTRACT

The study of quasi periodic oscillations (QPOs) plays a vital role in understanding the nature and geometry of the Comptonizing medium around black-hole X-ray binaries. The spectral-state dependence of various types of QPOs (namely A, B, & C) suggests that they could have different origins. The simultaneous presence of different types of QPOs would therefore imply the simultaneous occurrence of different mechanisms. In this work we study the radiative properties of two non-harmonically related QPOs in the black-hole binary GRO J1655–40 detected at the peak of the ultraluminous state during the 2005 outburst of the source. The two QPOs have been previously identified as types B & C, respectively. We jointly fit the phase-lag and rms spectra of the QPOs and the time-averaged spectrum of the source with the time-dependent Comptonization model `νKOMP` to infer the geometry of the media producing the QPOs. The time-averaged spectrum required a hot disk of 2.3 keV and a steep power law with index 2.7, revealing that the source was in an ultraluminous state. The corona that drives the variability of the type-B QPO is smaller in size and has a lower feedback fraction than the one that drives the variability of the type-C QPO. This suggests the simultaneous presence of a horizontally extended corona covering the accretion disk and a vertically elongated jet-like corona that are responsible for the type-C & B QPOs, respectively.

Key words: stars: individual: GRO J1655–40 – stars: black holes – X-rays: binaries – accretion, accretion discs

1 INTRODUCTION

The study of rapid aperiodic variability is a powerful tool in the characterisation of black-hole binaries. The time scales associated with the variability correspond to the motion of matter in the vicinity of the black hole (See reviews by Done et al. 2007; Ingram & Motta 2019, and references therein). Quasi periodic oscillations (QPOs), appearing as narrow peaks in the Fourier power spectra of these sources, are excellent tracers of the Comptonizing medium surrounding the black holes (van der Klis 1989; Nowak 2000; Belloni et al. 2002). Low-frequency QPOs (0.1 – 30 Hz) are classified into three sub categories, namely types A, B, and C, based on their centroid frequency, strength as well as the shape and variability of the broadband noise (Remillard et al. 2002; Casella et al. 2004).

Most black-hole binaries display outbursts during which the source goes from being undetected in the so-called quiescence, to a luminosity around the Eddington limit and back to quiescence on timescales of weeks to months (Lasota 2001; Frank et al. 2002). The ABC classification of QPOs plays an important role in characterising the different states of black-hole binaries (See e.g., Belloni 2010, for a review). A typical outburst begins in the low/hard state (LHS) where the hard Comptonized component, characterised by a shallow power-

law with an index of ~ 1.6 , dominates the spectrum. The fractional rms amplitude of the variability in the 0.1 – 20 Hz frequency range is high ($\sim 30\%$) and the power spectrum contains a type-C QPO (Psaltis et al. 1999; Belloni et al. 2002; Pottschmidt et al. 2003). As the luminosity increases, the source transitions to the high/soft state (HSS), via the hard (HIMS) and soft intermediate states (SIMS), with corresponding decrease in hardness and broadband variability. The power spectra in the HIMS also show type-C QPOs and the broadband noise have 10% – 20% rms amplitude. In the SIMS type-B or A QPOs are detected and the broadband noise further decreases to a few percent (Miyamoto et al. 1991; Belloni et al. 2005). While the time-averaged spectra of the two intermediate states are quite similar, with the power-law index lying around 2.0 – 2.4, the differences become clear in the power spectra (Gierliński & Zdziarski 2005). The HSS has the highest thermal disk contribution and the lowest variability, $\sim 1\%$ or less (Mitsuda et al. 1984; Belloni et al. 1999). Sometimes, type-A QPOs are detected during this state (Casella et al. 2004; Belloni 2010; Belloni & Motta 2016). The source stays in the HSS while the intensity decreases and then gradually transitions to the LHS via the same two intermediate states in reverse order. In the decay of an outburst, during the low-luminosity transitions, QPOs are sometimes detected, but less often than during the rise, generally owing to low count rates. Apart from these four standard states, sometimes the source makes an excursion to an anomalous or ul-

[★] E-mail: skROUT@prl.res.in (SKR)

traluminous state (ULS) just after or before the HSS (Belloni et al. 1997; Belloni 2010). Along with a manifold increase in luminosity, sometimes reaching and/or exceeding the Eddington rate, this state is characterised by low variability (5% – 10%) and large colour variations (Dunn et al. 2010; Uttley & Klein-Wolt 2015; Ingram & Motta 2019). During the ULS, the time-averaged spectrum remains very soft and the power spectrum shows type-B or C QPOs, thus inviting the moniker “anomalous” (Motta et al. 2012). The aforementioned states in black-hole binaries can be easily identified from the hardness-intensity diagram (Fender et al. 2004) and the absolute rms-intensity diagram (Muñoz-Darias et al. 2011). The changes of the source across spectral states are also accompanied by radio emission from a jet or a relativistic outflow (Fender et al. 2004). In particular, the transition from the HIMS to the SIMS usually coincides with the launch of relativistic jets that are bright in radio wavebands (Russell et al. 2019; Homan et al. 2020). The simultaneous detection of type-B QPOs and radio jets has inspired models explaining the former to be formed by the later (Kylafis et al. 2020).

With over three decades of extensive timing studies, the phenomenology of QPOs has become fairly clear, although the origin of the QPOs is still debated. The dynamic origin of the oscillations has been broadly ascribed to two categories of models, either due to the intrinsic variability of the accretion disk (Tagger & Pellat 1999; Molteni et al. 1996; Cabanac et al. 2010; Wagoner et al. 2001), or to geometrical effects (Stella & Vietri 1998; Ingram et al. 2009; Schnittman et al. 2006). These two classes of models are mostly concerned with the dynamic origin of the QPOs, answering basically how a particular frequency in the disk may be excited. While choosing one of the two categories is difficult, model-independent studies suggest a geometrical origin (Motta et al. 2015; van den Eijnden et al. 2017). These studies also claim a separate origin for the type-B and C QPOs. Ingram et al. (2016) carried out phase-resolved spectroscopy of the type-C QPO in H1743–322 that appears to indicate that the components of the reflection spectrum vary with the phase of the QPO, providing evidence for a geometrical origin. However, using the same technique on the type-C QPO in GRS 1915+105, Nathan et al. (2022) found a very small inner disk radius ($\sim 1.4 R_g$) and a very large thermalisation time scale (~ 70 ms). Such a small inner radius cannot accommodate the necessary inner flow for precession, while the large thermalisation time scale would wash out the short time lags observed in some cases. Stevens & Uttley (2016) carried out a similar exercise for the type-B QPO in GX 339–4, and they suggest a possible origin from precession of an extended jet (See also Kylafis & Reig 2018; Kylafis et al. 2020). Mastichiadis et al. (2022), on the other hand, showed that QPOs could be formed by a dynamic coupling between the accretion disk and the Comptonizing medium.

While much effort has been directed towards understanding the dynamical origin of the QPO, not much attention has been given to their radiative properties. Out of the few that have tried (e.g., Lee & Miller 1998; Lee et al. 2001; Shaposhnikov 2012; Nobili et al. 2000), most could explain only the energy-dependent phase-lags but not the rms amplitudes. Recently, Garg et al. (2020) developed a model incorporating propagation of fluctuations in the components of the time-averaged spectrum to qualitatively explain the time-lag and rms spectra of the QPOs in GRS 1915+105. Whatever the process behind the oscillations, it appears to be quite certain that the variability originates from the Comptonizing medium. This becomes evident as the QPOs are mostly detected in hard states, where Comptonization dominates the time-averaged spectrum and, furthermore, the rms of the QPOs generally increases with energy, in some cases reaching about 15% at 100 keV (Bu et al. 2021).

Karpouzas et al. (2020) built upon the Comptonization scheme of Lee & Miller (1998), Lee et al. (2001), and Kumar & Misra (2014) and developed a model to explain the radiative properties of QPOs in a neutron-star system. This model considers the QPOs to be oscillations of the thermodynamic properties of the accretion flow, such as the temperature and heating rate of the corona, and the seed photon temperature. The model incorporates feedback of a fraction of the Comptonized photons that return to the seed-photon source. Bellavita et al. (2022) extended the model by replacing the seed-photon source from a single temperature blackbody, relevant for neutron stars, to a multi-temperature blackbody, suitable for black-hole binaries. Using this model, named *vkompthdk*, the phase-lag and rms spectra of both type-B and type-C QPOs could be explained (García et al. 2021; Zhang et al. 2022, 2023; Peirano et al. 2023; Rawat et al. 2023). The results from these studies suggest that the geometry of the Comptonizing medium is different for the two types of QPOs. While in the case of type-B QPOs the corona has a vertically elongated (jet-like) geometry, the corona for type-C QPOs is more horizontally extended and significantly covers the accretion disk.

The two types of QPOs, B and C, mostly appear in separate states, it is only in rare cases that they appear together. If their origin are indeed from separate structures, as found earlier, simultaneous type-B and C QPOs would imply a complex structure of the corona with both vertically elongated and horizontally extended components. To test this hypothesis, we study the simultaneous type-B and C QPOs detected during the ULS of GRO J1655–40 (henceforth, J1655) during its 2005 outburst (Debnath et al. 2008; Motta et al. 2012). This outburst was densely monitored by the Rossi X-ray Timing Explorer (RXTE), showing that the source traced all spectral states. Following the HSS, for about twenty days, J1655 made an excursion to the ULS that was apparent in the hardness-intensity diagram as a huge increase in count rate along with marginal increase in hardness and variability. The power spectrum during this state consisted of a type-C QPO along with a broad peak with a similar frequency-rms relation as that for type-B QPOs (Motta et al. 2012). When the source reached the peak luminosity within the ULS (and also overall), the broad power-spectral peak transitioned into a proper type-B QPO. The observation during that period, dated 2005 May 18 (ObsID 91702015800), consisting of both a type-B and C QPO is analysed here. In Section 2 we describe the data reduction and analysis methods. In Section 3 we present the main result from the simultaneous fits to the time-averaged spectrum of the source and the rms and phase-lag spectra of the QPOs. Finally, in Section 4 we discuss the implications of the result of our analysis on the origin of the QPOs and the geometry of the Comptonizing medium.

2 DATA REDUCTION AND ANALYSIS

We reduced the Proportional Counter Array (PCA) binned data using the new tools in *heasoft*-6.31. The new tools are a wrapper of the old extraction tools making the analysis simpler. We extracted the source spectrum in the 3–30 keV range from the *Standard 2* mode using all standard filtering criteria. We selected the data from all three xenon layers of the Proportional Counter Unit (PCU) 2 for the source spectrum. We computed the background spectrum using the bright background model *pca_bkgd_cmv1e_eMv20111129.mdl*.

We carried out the timing analysis with the IDL-based timing package *GHATS*¹. The high time resolution PCA data were packaged

¹ http://astrosat.iucaa.in/~astrosat/GHATS_Package/Home.html

in two single bit modes with $125 \mu\text{s}$ resolution and one event mode with $62 \mu\text{s}$ resolution. The single bit mode data were binned into two broad channel ranges, one spanning channels 0 to 13 ($2.06 - 7.35 \text{ keV}$) and the other covering channels 14 to 35 ($7.46 - 16.43 \text{ keV}$). The event mode, on the other hand, consisted of 32 channels from 36 to 249. We constructed the broadband power spectrum by averaging over the full $3 - 30 \text{ keV}$ lightcurve segments of 16 s and a time resolution of $1/4096 \text{ s}$ giving a Nyquist frequency of 2048 Hz . We removed the Poisson noise by subtracting the average power between $1000 - 2000 \text{ Hz}$ from the Leahy normalized power spectrum. We then converted the normalization to squared fractional rms following Belloni & Hasinger (1990). We fitted the power spectrum by a multi-Lorentzian model in *xspec* (Belloni et al. 2002). The model required five Lorentz components to fit the $0.01 - 100 \text{ Hz}$ spectrum. Out of these Lorentzians, three fitted the broadband noise and two were required for the QPOs. The lower frequency QPO at 6.8 Hz is the type-B QPO and the higher frequency QPO at 19.0 Hz is the type-C QPO (Motta et al. 2012).

We constructed the rms spectra for each of the two QPOs by extracting the power spectra for smaller energy bins and fitting them with the same multi-Lorentzian model that we used for the full band. While computing the rms we fixed the centroid frequency and the full width at half maximum (FWHM) to the values obtained from fitting the full band. It was possible to make significant measurement for six energy bins in the $2 - 30 \text{ keV}$ range. The common way to compute the phase lags of QPOs is to average the real and imaginary part of the cross-spectrum in a frequency range dominated by the QPO signal, usually the FWHM of a QPO. This works well when the QPO is very strong and not contaminated by other components. The two QPOs in the power spectrum of J1655 are quite close to each other and their respective Lorentzians have significant overlap, both with each other and with Lorentzians of the adjacent continuum (Figure 1). Therefore, we use a novel technique to extract the phase-lags from the entire region of the power spectrum where the QPO is present (Peirano & Méndez 2022; Alabarta et al. 2022). We constructed the cross spectra using the full energy band as the reference band and the six smaller energy bins used for the rms spectra as the subject bands. We jointly fitted the real and imaginary parts of the cross spectra with a multi-Lorentzian model. We also fitted a constant to the real part of the cross-spectrum to account for the cross-correlation introduced from using the full band as reference. Apart from that we introduced an additive model using *mdefine* with a single parameter for capturing the phase-lag ($\Delta\Phi$). We fixed the frequency and FWHM of the Lorentzians to the values obtained from fits to the full energy power spectrum. The normalization of the real part was left free to vary while that of the imaginary part was linked to the phase-lag as $\text{Im}(C) = \text{Re}(C) \times \tan(\Delta\Phi)$ where C is the complex cross-spectrum. In this way the phase-lag is obtained as an *xspec* parameter and takes into account the entire profile of the QPO in the full frequency range.

With all the products ready we jointly fitted the fractional rms and phase-lag spectra of both QPOs along with the time-averaged energy spectrum of the source. The time-averaged spectrum required the typical combination of an absorbed (TBabs) disk (diskbb; Mitsuda et al. 1984), Comptonization (nthComp; Zdziarski et al. 1996; Życki et al. 1999) and reflection (relxillCp; Dauser et al. 2014; García et al. 2014) components. We adopted the abundance in the TBabs component from Wilms et al. (2000) and set the cross-sections according to Verner et al. (1996). We fixed the neutral H column density to $7.5 \times 10^{21} \text{ cm}^{-2}$ (Díaz Trigo et al. 2007; Brocksopp et al. 2006). The diskbb component represents the emission of a multi-temperature blackbody based on the α -disk prescription of Shakura & Sunyaev

(1973) and is parameterised by the inner-disk temperature (kT_{in}) and a normalization (N_{dbb}). The Comptonization component nthComp is approximately equal to a power law with index Γ , along with a high energy cutoff and a low energy rollover. The high energy cutoff is parameterised by the electron temperature, kT_e , and the low-energy rollover by the seed photon temperature, kT_{bb} , which in our case was tied to kT_{in} from diskbb. nthComp has a switch *inp_type* to toggle between a single temperature blackbody relevant for neutron star binaries and a disk blackbody pertinent for black hole binaries. We chose the later. relxillCp is a relativistic reflection model with the irradiating flux, or emissivity, assumed to be a broken power law. The outer emissivity index was fixed to the Newtonian value of 3 and the break radius was fixed at $6 R_g$. The inner emissivity index, $q1$, was allowed to vary within $3 - 10$. The primary source spectrum is the same as nthComp, therefore, we tied Γ and kT_e parameters in relxillCp to the respective parameters in nthComp. Since we had separately included a Comptonization component, the *refl_frac* parameter was fixed at -1 letting relxillCp to contribute only the reflection part. We fixed the Fe abundance at solar values and left the disk density and ionization parameters free to vary.

We fitted the phase-lag and rms spectra of the QPOs with the time-dependent Comptonization model vkompthdk (Bellavita et al. 2022). This variant incorporates diskbb as the seed-photon source and considers a single corona. The time-averaged version of vkompthdk is essentially the same as nthComp. We tied the seed-photon temperature, power-law index, and coronal temperature in vkompthdk to the kT_{in} of diskbb and Γ and kT_e of nthComp, respectively. The model is broadly insensitive to the *af* parameter. We verified that by tying *af* to the inner disk radius obtained from the normalization of diskbb (Makishima et al. 1986; Kubota et al. 1998). The fit statistics and the best-fitting parameters remained unaffected. Therefore, we fixed *af* to the default value of 250 km . Apart from these, vkompthdk has the coronal size, L , the feedback fraction, η , the variability in the external heating rate of the corona, $\delta\dot{H}_{ext}$, and an additive reference lag, *reflag*, as free parameters. *reflag* is the lag of the model in the $2 - 3 \text{ keV}$ band and adjusts the lag to account for the fact that the lag spectrum is defined except for an additive constant. This allows the user to choose the reference band arbitrarily. The feedback fraction, $0 \leq \eta \leq 1$, is given as

$$\eta = \frac{F_{D,f} - F_{D,o}}{F_{D,f}}$$

where $F_{D,f}$ is the flux of the disk after it has thermalised the irradiated hard photons from the corona and $F_{D,o}$ is the flux of the disk before the corona illuminates it. Thus, η represents the fraction of the total disk flux that arises due to the feedback of coronal photons. Internally, however, the model calculates an intrinsic feedback fraction, η_{int} , which is the fraction of Comptonized photons that illuminates the disk (Karpouzas et al. 2020). The η_{int} is not a free parameter in the model as its maximum attainable value changes with the disk and the coronal parameters, which makes it impractical to use it in *xspec*.

Owing to the low resolution of the PCA spectrum, the spin and inclination parameters in relxillCp cannot be constrained. Therefore we strove to fix these parameters to the best estimates from the literature. However, there are multiple contradicting reports making the choice tricky. By modeling the three simultaneous QPOs with the relativistic precession model, Motta et al. (2014) and Rink et al. (2022) arrived at a low spin $a \sim 0.3$. Shafee et al. (2006) reported a spin $a = 0.7$ from continuum fitting, while Reis et al. (2009) measured $a > 0.9$ using reflection spectroscopy. Reis et al. (2009) noted that the spin will be greater than 0.9 using continuum fitting after using the correct distance. A high spin was further suggested by Díaz

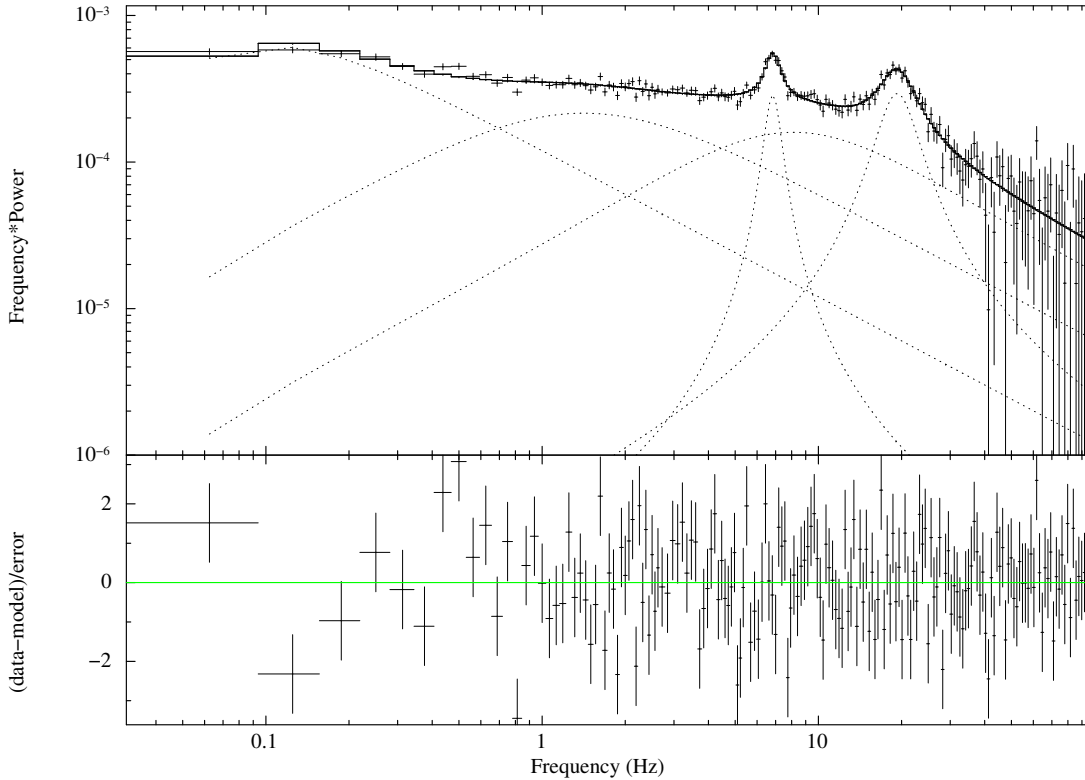


Figure 1. Top panel: The power spectrum of GRO J1655–40 fitted with a multi-Lorentzian model. The dotted lines are the individual Lorentzian components used in the fitting. The solid line represents the total model. The peak at ≈ 7 Hz is the type-B QPO and the peak at ≈ 20 Hz is the type-C QPO. Bottom panel shows the residuals of the fit.

Trigo et al. (2007) based on reflection fits with a relatively high inclination. Stuchlík & Kološ (2016) attempted to address the conflicting spin estimates and found that by using an epicyclic resonance model, and abandoning the assumption that all QPOs originate at a single radius, the spin from QPOs can become consistent with the Fe line results. Deciding the true inner disk inclination is even more complicated. While the orbital inclination was found to be 70° (Greene et al. 2001), the jet was reported to be tilted at 85° (Hjellming & Rupen 1995) suggesting spin-orbit misalignment. However, with reflection spectroscopy the inclination was found to be 30° (Reis et al. 2009) or 52° & 63° (Díaz Trigo et al. 2007). With such a variety of options it is only meaningful to try different combinations and see how the data respond.

One important aspect to be dealt with is that the `vkompthdk` model is a purely Comptonization model whereas the time-averaged spectrum consists of significant contribution from the disk and reflection components. Therefore, the rms calculated by the model is only from the Comptonized component, whereas the observed rms will be diluted by the effects of the disk and reflection, which are assumed to be much less variable than the corona. To take into account this effect we multiplied a `dilution` component to `vkompthdk` only for the rms spectra. The dilution is defined as the fraction of the total flux

contributed by the `nthComp` component, $\text{nthComp}(E)/(\text{diskbb}(E) + \text{nthComp}(E) + \text{relxillCp}(E))$ (Bellavita et al. 2022).

3 RESULTS

We show the 0.03 – 100 Hz power spectrum of J1655 in Figure 1. The power spectrum has a flat top spanning about three decades in frequency and falls off at around 20 Hz. It can be decomposed into five Lorentzians and has a broadband 0.03 – 100 Hz fractional rms of 5.4%. Out of the five components, three Lorentzians account for the broad continuum and the other two fit the QPOs at 6.8 Hz and 19.0 Hz. The former is a type-B QPO and the later is a type-C QPO having fractional rms amplitudes of 0.8% and 1.2%, respectively. The simultaneity of the two QPOs is demonstrated by the spectrogram shown in Figure 2. This classification is based on the fact that the two QPOs lie on the two branches corresponding to the types-B and C on the broadband rms - QPO frequency plane and the type-B QPO at 6.8 Hz is highly variable in frequency (See Figure 5 in Motta et al. 2012). While this classification helps in contextualizing our work within the existing literature, it is worth noting that our conclusion is independent of the QPO classification.

Deciphering the radiative origin of these two QPOs is the objective

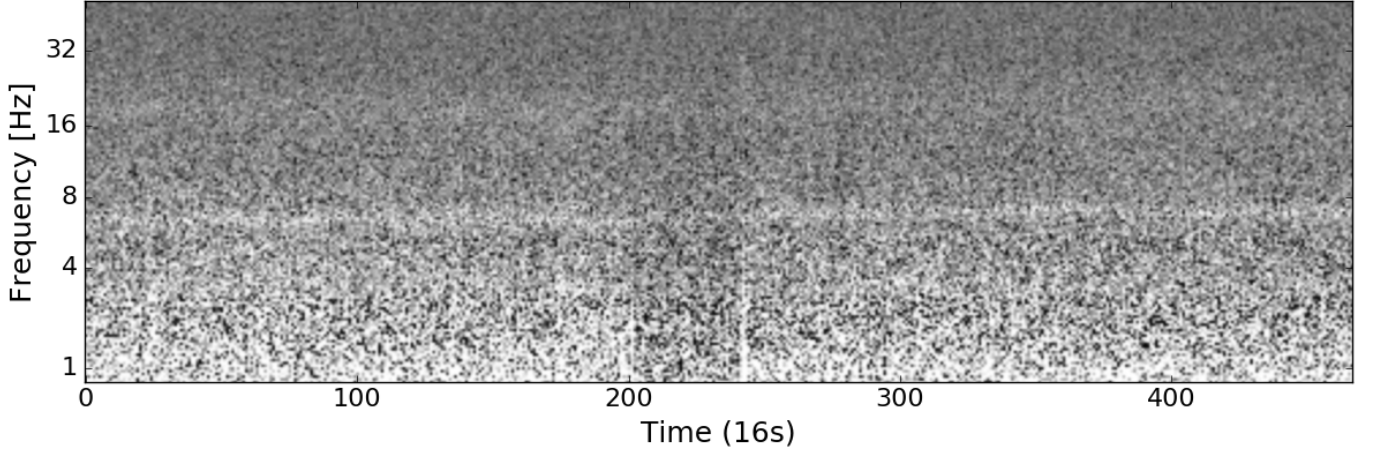


Figure 2. Spectrogram for the observation showing the two simultaneous QPOs at 6.8 Hz and 19 Hz. Each bin in the time axis spans 16 seconds.

of this work. The time-averaged spectrum of the source and the fractional rms and phase-lag spectra of the QPOs were jointly fitted in *xspec*. As explained in detail in section 2, the PCA spectrum could not discriminate between the low (0.3) and high (0.9) spin values, yielding an acceptable fit in both cases. However, the inclination seemed to be correlated to the spin, with a lower spin giving a low inclination ($\sim 30^\circ$) and a higher spin leading to a high inclination ($\sim 50^\circ$) when left free. Trying to freeze the inclination to the orbital tilt (70°) or the jet orientation (85°) did not result in acceptable fits. Instead, leaving the spin free with the inclination fixed at 70° gave an acceptable fit, albeit with a much higher spin estimate of ~ 0.99 . It is worthwhile to remember that reflection spectroscopy with XMM-Newton data also resulted in very similar spin and inclination estimates (Reis et al. 2009; Díaz Trigo et al. 2007).

Table 1 gives the best-fitting parameters with three variations of the model by fixing the spin and inclination to different values. Two combinations involve fixing the spin to 0.3 and 0.9 while keeping the inclination free, while the third combination keeps the inclination fixed at 70° and allows the spin to vary. The errors quoted represent 1σ uncertainty and were evaluated by running Markov Chain Monte Carlo simulations in *xspec* with 1000 walkers and 2×10^5 steps with an initial burn-in length of 40000 steps to ensure the convergence of the chains. We re-scaled the covariance matrix by 10^{-4} in order to sample a wide parameter space by the walkers. It is apparent that most of the best fitting parameters remain consistent across the three variants of the models. The only significant differences are the fluxes of the individual components of Model 3 ($i = 70^\circ$) which are different from those of Models 1 & 2. Apart from these the inner disk temperature and disk ionization parameter are, respectively, slightly higher and lower in Model 3 than in Models 1 & 2. The high disk temperature $kT_{in} \sim 2.4$ keV and photon index, $\Gamma \sim 2.7$, confirms the ultra soft nature of the source during the observation. The electron temperature could not be constrained for Models 2 & 3, pegging at the upper limit of 250 keV. For model 1, kT_e was constrained to

≈ 208 keV. From the reflection component, we found that both the inner emissivity power-law index (≥ 8) and disk ionization ($\geq 10^{3.5}$ erg cm s $^{-1}$) remained high. The disk density, on the other hand, was constrained to moderate values of $N \sim 10^{16.5}$ cm $^{-3}$. Figure 3 shows the fitted time-averaged spectrum of the source and the rms and phase-lag spectra of the QPOs for the Model 2.

The remarkable result of the joint fitting exercise is that the parameters pertaining to the coronal geometry from *vkompthdk* remained consistent across the three model variants. The corona responsible for the type-B QPO has a size of ≈ 680 km and a low feedback fraction of $\sim 10\%$. For the type-C QPO, on the other hand, the corona is much larger, with a size of ≈ 1150 km and the feedback fraction is also high at $\sim 60\%$. The corresponding intrinsic feedback fractions, η_{int} , are $\sim 4\%$ and $\sim 16\%$ for the type-B and C QPOs, respectively. The external heating rate for both QPOs is similar, varying between 0.05 - 0.1. Finally, the reduced χ^2 indicate that all three models provide excellent fits and it is not possible to choose one over the other. We can conclude that a particular choice of the spin and inclination does not drastically affect the joint fits. Most importantly, the geometry of the corona obtained from *vkompthdk* remains completely unaffected. In Figure 4 we show the confidence contours of the relevant coronal parameters (i.e., size and the feedback fraction) obtained by carrying out Monte Carlo simulations for Model 2. The corresponding contours from Model 1 & 3 are almost identical to those of Model 2. The contours for η_1 appears to be bimodal, however, the separation of the two lobes is merely at a few percent level.

4 DISCUSSION

The power spectrum of J1655 at the peak of the ultraluminous state during its 2005 outburst displays two non-harmonic QPOs (Figure 1), which were identified as being types-B & C (Motta et al. 2012). We jointly fitted the time-averaged spectrum of the source and the phase-

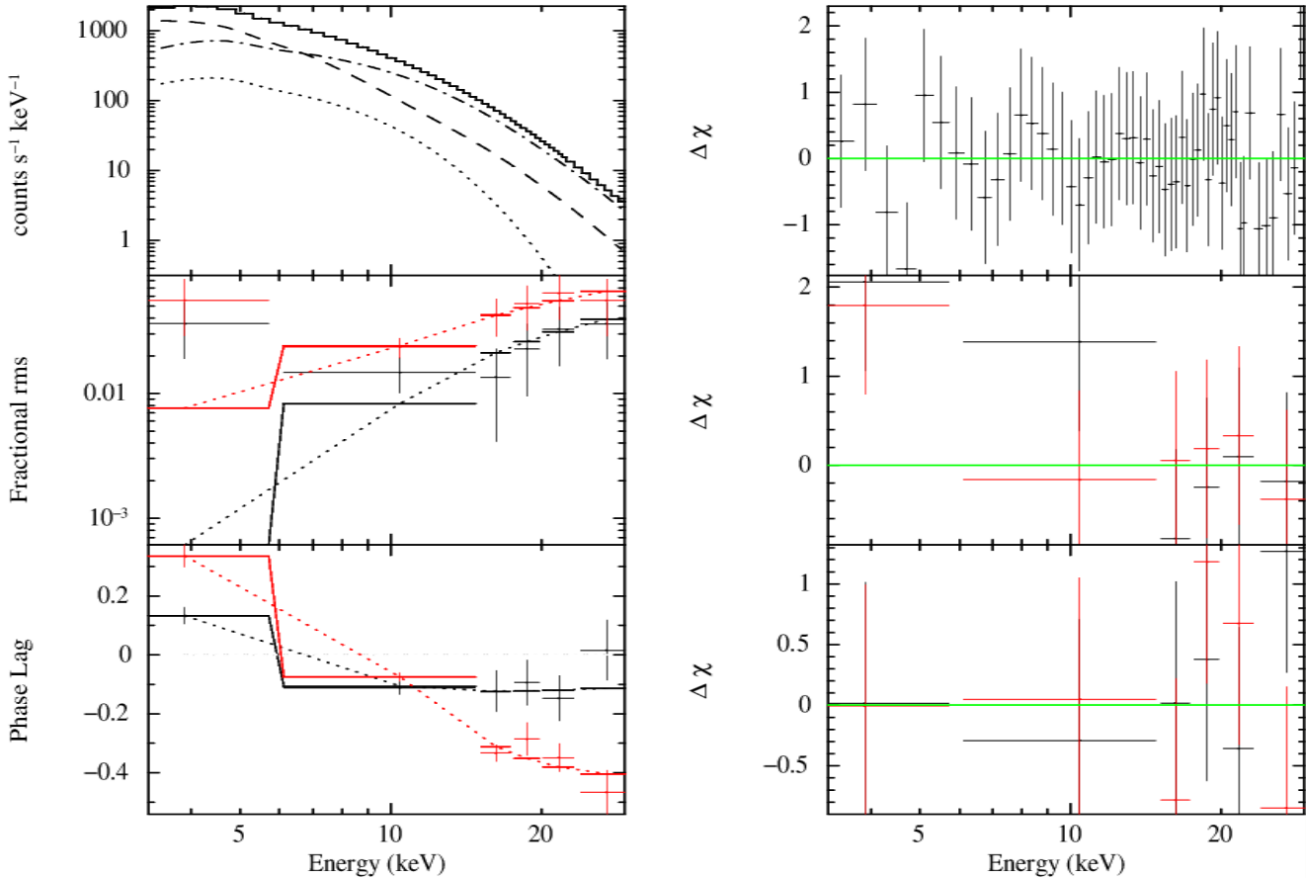


Figure 3. From top to bottom, the left panels represent, respectively, the time-averaged spectrum of the source and the fractional rms and phase-lag spectra of the QPOs. The corresponding panel in the right column are the residuals. The black and red points in the middle and bottom panels represent the type-B and C QPO, respectively. The dotted lines are the best-fitting models. In the top left panel, the dotted, dashed, and dot-dashed lines represent the disk, Comptonization, and reflection components, respectively.

lag and rms spectra of the QPOs to infer the radiative origin of the QPOs. The phase-lag and rms spectra were modeled with the recently developed time-dependent Comptonization model *vkompthdk* (Karpouzas et al. 2020; Bellavita et al. 2022). The type-B QPO required a corona of size ≈ 680 km and an intrinsic feedback of $\sim 4\%$. The type-C QPO, on the other hand, required a coronal size of ≈ 1150 km and a higher feedback of $\sim 16\%$. Using only spectral-timing methods, we show for the first time the co-existence of a vertically elongated, or jet-like corona, and a horizontally extended, or slab-like corona, the oscillations of which result in the type-B and C QPOs, respectively.

Hard X-rays in black-hole binaries are produced by inverse Compton scattering of disk photons in an optically thin cloud of electrons known as the corona (Sunyaev & Truemper 1979). Since the variability amplitude increases with energy, Sobolewska & Życki (2006) posited that the radiative properties of the power spectral components should have their origin in the corona. The most prominent of these variability components are QPOs, which appear as narrow peaks in the power spectrum. The QPOs are classified into types A, B, & C based on their frequency and other variability properties (See Section 1). The different types of QPOs have different lag/rms spectra and thus believed to originate from different parts of the corona or a corona with properties that change as the source moves through different states. The increase in rms with energy for both the QPOs (Figure 3), however, suggests a common process likely connected with inverse Comptonization. The same process also gives rise to

hard time lags since the hard photons, having undergone Comptonization, arrive later than the soft seed photons (Miyamoto et al. 1988). Sometimes a fraction of these scattered hard photons travels back and gets thermalised in the accretion disk. Whenever this newly thermalised photons dominate over the intrinsic emission of the disk, the soft photons will arrive later than the hard photons resulting in a soft lag (Uttley et al. 2011, 2014; De Marco et al. 2015).

The appearance of the QPOs in the ULS indicates a peculiar change in the accretion flow. In the state transition scheme of black hole binaries, the ULS is both preceded and followed by the HSS. During the HSS, the corona likely disappears indicated by an increase in the fraction of the disk flux, the disappearance of QPOs, and a decrease in the total fractional variability. The re-appearance of the QPOs during the ULS suggests the restoration of the corona for a short period. It is noteworthy that the two QPOs simultaneously occurring suggests a common emission mechanism for the two, despite different dynamical origins. This is precisely the assumption in the *vkompthdk* model where all kinds of QPOs are generated by the same process of inverse Comptonization. The fact that the lags are different for the two QPOs (See Figure 3) suggests that the photons travel through regions with different geometrical properties, which makes their radiative properties different.

The *vkompthdk* model used in this work includes a feedback loop akin to the physical scenario where a fraction of the hard coronal photons return to the disk and are re-emitted, accounting for the soft lags. The fraction of the primary hard emission that returns to the

Table 1. The best-fitting parameters from the simultaneous fit to the time-averaged spectrum of the source and the rms and lag spectra of the QPOs. The three models correspond to the three choices of spin and inclination as mentioned in the top row. The η_{int} is not a model parameter and it is computed separately. The errors represent the 1σ uncertainty.

Component	Parameter	Model 1 $a = 0.3$ i free	Model 2 $a = 0.9$ i free	Model 3 a free $i = 70^\circ$
diskbb	kT_{in} (keV)	2.38 ± 0.01	2.35 ± 0.04	2.44 ± 0.03
	$norm$	24.0 ± 0.2	$23.8^{+1.5}_{-1.2}$	$32.1^{+3.2}_{-2.3}$
nthComp	Γ	2.739 ± 0.003	2.76 ± 0.01	2.76 ± 0.01
	kT_e (keV)	$207.6^{+3.7}_{-4.9}$	> 199	> 198
	$norm$	$3.21^{+0.08}_{-0.04}$	3.4 ± 0.2	2.9 ± 0.1
relxillCp	i ($^\circ$)	$23.4^{+0.1}_{-0.5}$	51.7 ± 1.2	-
	a	-	-	0.990 ± 0.001
	$q1$	> 9.7	8 ± 1	> 9.7
	$\log \xi$ (erg cm s $^{-1}$)	4.46 ± 0.01	4.28 ± 0.07	3.5 ± 0.1
	$\log N$ (cm $^{-3}$)	16.51 ± 0.03	16.45 ± 0.10	16.7 ± 0.1
	$norm$	$0.762^{+0.003}_{-0.007}$	1.33 ± 0.05	2.7 ± 0.1
vkompthdk (Type-B QPO)	L (km)	707^{+31}_{-15}	676^{+97}_{-92}	660^{+81}_{-58}
	η	0.141 ± 0.002	$0.138^{+0.004}_{-0.022}$	0.15 ± 0.01
	η_{int}	0.038 ± 0.001	$0.037^{+0.002}_{-0.006}$	$0.041^{+0.001}_{-0.005}$
	$\delta\dot{H}_{\text{ext}}$	0.051 ± 0.001	0.055 ± 0.009	0.06 ± 0.01
	$reflag$	0.90 ± 0.07	$1.3^{+0.9}_{-0.4}$	$0.98^{+0.29}_{-0.37}$
vkompthdk (Type-C QPO)	L (km)	1153^{+5}_{-10}	1148^{+70}_{-58}	1137^{+39}_{-33}
	η	0.59 ± 0.01	0.60 ± 0.05	0.59 ± 0.03
	η_{int}	0.157 ± 0.008	0.16 ± 0.02	0.16 ± 0.02
	$\delta\dot{H}_{\text{ext}}$	0.083 ± 0.002	0.09 ± 0.01	0.10 ± 0.01
	$reflag$	0.44 ± 0.01	0.45 ± 0.04	0.45 ± 0.02
χ^2/dof		46.46/60	41.98/60	38.91/60

disk, which is parameterized in the model as η , can be used as a proxy for the geometry of the Comptonizing medium (Méndez et al. 2022; García et al. 2022). A higher feedback fraction implies that the disk is enveloped by the Comptonizing medium, increasing the chance of back scattered photons to impinge onto the disk. This can happen when a horizontally extended corona covers a significant part of the disk. Accordingly, a lower feedback fraction would mean that the corona and the disk are spatially separated in such a way that the back scattered photons find it difficult to reach the disk. A vertically elongated or jet-like geometry of the corona could explain the low feedback fraction. The vkompthdk model assumes a spherical and homogeneous corona of uniform density and electron temperature. Despite this simplified picture, which is necessary for solving the equations, it is remarkable that the model is able to explain the radiative properties of different types of QPOs.

The size of the corona and the feedback fraction are mainly constrained by the phase-lag spectra of the QPOs. While the amplitude of the lags constrains the size, the relative sign of the lags constrains the feedback fraction. This is intuitive, as a larger corona would imply that the seed photons spend more time inside the corona resulting in longer lags. Accordingly, a negative lag implies that the Comptonized photons scatter back and impinge the disk which re-emits thermally after the correlated coronal emission. This can happen when the corona physically envelopes the disk. Conversely, a positive lag indicates a geometry where the corona is physically detached, or far away, from the disk so that feedback is difficult to manifest. The phase-lag spectra of the two QPOs in J1655 (Figure 3) clearly discerns these two scenarios. The phase-lag spectrum of the type-B QPO is flat and has a low amplitude, whereas the phase-lag spectrum of the type-C QPO is inverted, with negative lags increasing with energy.

This suggests that the type-B QPO originates from a smaller corona which is detached from the disk and the type-C QPO arises from a bigger corona which envelopes the disk so as to facilitate higher feedback. The best-fit parameters from our fits with the vkompthdk model correspond quite well with this geometry (See Table 1). The type-B QPO is produced by a corona of ≈ 680 km and an intrinsic feedback fraction of $\sim 4\%$ while the type-C QPO comes from a larger corona of ≈ 1150 km and a relatively higher intrinsic feedback of $\sim 16\%$. This would mean the simultaneous presence of two different coronal geometries during the observation. The type-C QPO originates from the oscillations in a larger, horizontally extended, corona while the type-B QPO arises from oscillations in a smaller, vertically elongated, or jet-like, corona. Figure 5 represents schematically the scenario described here, where two physically distinct Comptonizing media are simultaneously present. The vkompthdk model used here is oblivious to the physical origin of the dynamics of the QPOs. It only explains the radiative origin by assuming the coronal and disk properties to oscillate at the QPO frequency. The oscillations could arise either due to geometrical factors or intrinsic variability (Section 1). Mastichiadis et al. (2022) recently showed that the QPOs could be dynamically produced by a resonant coupling between the accretion disk and the hot Comptonizing corona, which is in agreement with the assumptions of vkompthdk. Although the reflection component was significant, using the PCA spectrum we were not able to constrain the spin of the black hole and the inclination of the disk by fitting the relativistic Fe K α line. We verified that fixing the spin parameter to 0.3 (Motta et al. 2014) or 0.9 (Reis et al. 2009; Stuchlík & Kološ 2016) while allowing the inclination to vary, or fixing the inclination to 70° (Greene et al. 2001) while varying the spin gives identical fits. Not only are the three variants statistically similar, but

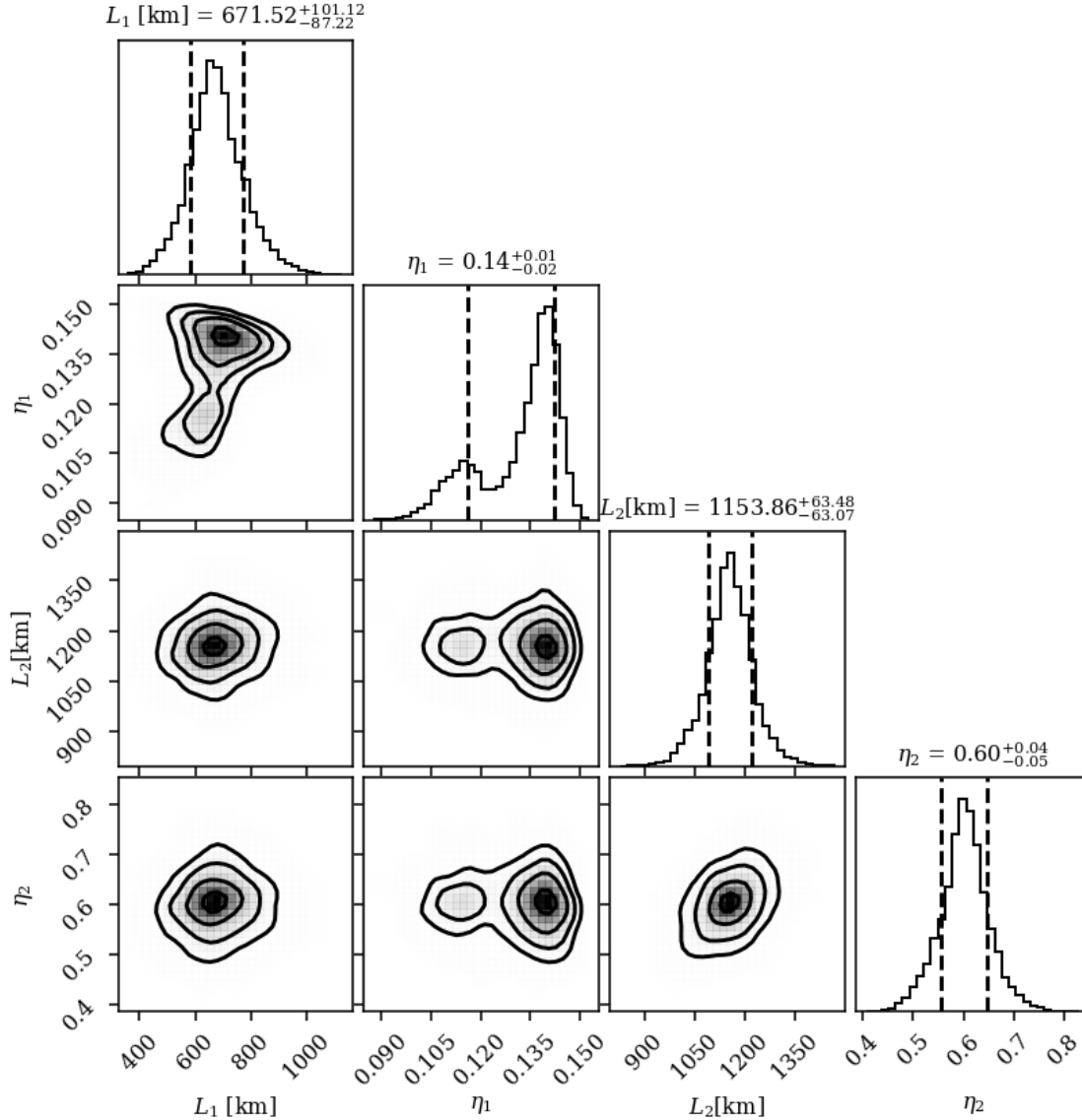


Figure 4. The confidence contours of the geometry parameters (size, L , and feedback fraction, η_1) from the best fit with the `vkompthdk` model-2. The 1 and 2 subscripts represent the type-B and C QPO, respectively. The corner plot is generated using the tool `pyXspecCorner`.

the best-fitting parameters are also consistent with being the same (Table 1).

There is increasing evidence that the type-B QPOs are associated with the jet emission (Fender et al. 2009; Homan et al. 2020; García et al. 2021). The transition from the HIMS to the SIMS is marked by both the appearance of a type-B QPO and ejection of a relativistic jet (Fender et al. 2004; Russell et al. 2019; Homan et al. 2020). The type-B QPO variability has also been seen to correlate with the system inclination, suggesting a jet origin (Motta et al. 2015; Reig & Kylafis 2019). Kylafis et al. (2020) were able to explain the variability of the photon index of the Comptonizing component by considering the Comptonization to take place in a precessing jet. On the other hand, the type-C QPOs have been shown to originate from an extended corona. For instance, the geometrical model for the formation of type-C QPOs considers the oscillations to arise from a precessing inner accretion flow (Ingram et al. 2009). Recently, polarization measurement of Cyg X-1 in the hard state indicated a horizontally extended, slab-like, corona (Krawczynski et al. 2022).

Since during the hard states we generally detect type-C QPOs, we can associate them with a horizontally extended corona, akin to what we got for J1655.

Previous studies using the `vkompthdk` model (and its dual-component variant `vkdua1dk`) are broadly consistent with the aforementioned idea. The evolution of the type-C QPOs during the HIMS in MAXI J1535–571 shows that the corona size initially decreases and then increases rapidly towards the end of the HIMS. The feedback fraction, on the other hand, evolves conversely suggesting that the corona transformed from a horizontal to a vertical structure (Rawat et al. 2023; Zhang et al. 2022). Towards the end of the HIMS, the corona of MAXI J1535–571 reached its maximum size. The transition from the HIMS to the SIMS was coincidental with the ejection of a transient jet and the appearance of type-B QPOs. Zhang et al. (2023) analyzed these type-B QPOs and showed that the corona contracted in the vertical direction, and the feedback fraction gradually increased along the SIMS. The type-B QPOs in MAXI J1348–630 and GX 339–4 have been shown to require two physically connected

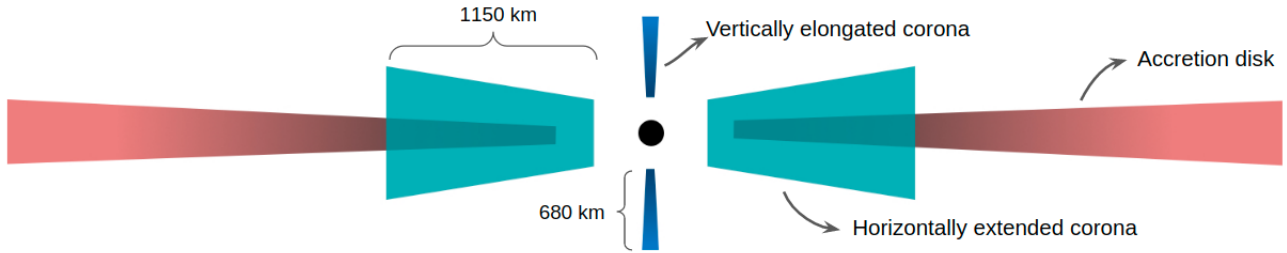


Figure 5. A schematic of the geometry of the two coronae simultaneously present during the observation. Comptonization in the vertically elongated jet-like corona resulted in the type-B QPO while Comptonization in the horizontally extended corona led to the type-C QPO.

structures (García et al. 2021; Bellavita et al. 2022; Peirano et al. 2023). Often the larger of the two structures is interpreted as a jet and the smaller structure, with a higher feedback fraction, is associated with a compact corona. These studies with the dual-component model (vkdualdk) suggest that the corona harbours a complex geometry with the presence of both a horizontal and vertical structure. Depending on the strength of their variability, one or both the structures manifest themselves in the data. Recently, Méndez et al. (2022) found a strong connection between the corona and the jet in GRS 1915+105, suggesting that the former morphs into the later due to a redistribution of the accretion power. While they observed only type-C QPOs during the HIMS, the changes in the corona could be due to the source approaching the SIMS. Since type-B QPOs were not detected, the source probably never made the transition to the SIMS. Our analysis of J1655 during the ULS demonstrates one such rare instance when the transition has taken place and both the corona and the jet are simultaneously present.

ACKNOWLEDGEMENTS

SKR acknowledges the support of the COSPAR fellowship programme for partially funding a visit to the University of Groningen which culminated in this research. SKR also acknowledges the support of Physical Research Laboratory which is funded by Department of Space, Government of India. MM and FG have benefited from discussions during Team Meetings of the International Space Science Institute (Bern), whose support they acknowledge. MM and FG acknowledge the research programme Athena with project number 184.034.002, which is (partly) financed by the Dutch Research Council (NWO). FG is a CONICET researcher and acknowledges support by PIBAA 1275 and PIP 0113 (CONICET).

DATA AVAILABILITY

The X-ray data used in this article are accessible at NASA's High Energy Astrophysics Science Archive Research Center <https://heasarc.gsfc.nasa.gov/>. The time-dependent Comptonization model and the generator of the MCMC corner plot are available at the GitHub repositories <https://github.com/candebellavita/vkompth> and <https://github.com/garciafederico/pyXspecCorner>.

REFERENCES

Alabarta K., Méndez M., García F., Peirano V., Altamirano D., Zhang L., Karpouzas K., 2022, *MNRAS*, **514**, 2839
Bellavita C., García F., Méndez M., Karpouzas K., 2022, *MNRAS*, **515**, 2099

Belloni T. M., 2010, *States and Transitions in Black Hole Binaries*. Springer-Verlag, Berlin, p. 53, doi:10.1007/978-3-540-76937-8_3
Belloni T., Hasinger G., 1990, *A&A*, **230**, 103
Belloni T. M., Motta S. E., 2016, *Transient Black Hole Binaries*. Springer, p. 61, doi:10.1007/978-3-662-52859-4_2
Belloni T., Méndez M., King A. R., van der Klis M., van Paradijs J., 1997, *ApJ*, **488**, L109
Belloni T., Méndez M., van der Klis M., Lewin W. H. G., Dieters S., 1999, *ApJ*, **519**, L159
Belloni T., Psaltis D., van der Klis M., 2002, *ApJ*, **572**, 392
Belloni T., Homan J., Casella P., van der Klis M., Nespoli E., Lewin W. H. G., Miller J. M., Méndez M., 2005, *A&A*, **440**, 207
Brocksopp C., et al., 2006, *MNRAS*, **365**, 1203
Bu Q. C., et al., 2021, *ApJ*, **919**, 92
Cabanac C., Henri G., Petrucci P. O., Malzac J., Ferreira J., Belloni T. M., 2010, *MNRAS*, **404**, 738
Casella P., Belloni T., Homan J., Stella L., 2004, *A&A*, **426**, 587
Dauser T., García J., Parker M. L., Fabian A. C., Wilms J., 2014, *MNRAS*, **444**, L100
De Marco B., Ponti G., Muñoz-Darias T., Nandra K., 2015, *ApJ*, **814**, 50
Debnath D., Chakrabarti S. K., Nandi A., Mandal S., 2008, *Bulletin of the Astronomical Society of India*, **36**, 151
Díaz Trigo M., Parmar A. N., Miller J., Kuulkers E., Caballero-García M. D., 2007, *A&A*, **462**, 657
Done C., Gierliński M., Kubota A., 2007, *A&ARv*, **15**, 1
Dunn R. J. H., Fender R. P., Körding E. G., Belloni T., Cabanac C., 2010, *MNRAS*, **403**, 61
Fender R. P., Belloni T. M., Gallo E., 2004, *MNRAS*, **355**, 1105
Fender R. P., Homan J., Belloni T. M., 2009, *MNRAS*, **396**, 1370
Frank J., King A., Raine D. J., 2002, *Accretion Power in Astrophysics: Third Edition*. Cambridge University Press, Cambridge, UK
García J., et al., 2014, *ApJ*, **782**, 76
García F., Méndez M., Karpouzas K., Belloni T., Zhang L., Altamirano D., 2021, *MNRAS*, **501**, 3173
García F., Karpouzas K., Méndez M., Zhang L., Zhang Y., Belloni T., Altamirano D., 2022, *MNRAS*, **513**, 4196
Garg A., Misra R., Sen S., 2020, *MNRAS*, **498**, 2757
Gierliński M., Zdziarski A. A., 2005, *MNRAS*, **363**, 1349
Greene J., Bailyn C. D., Orosz J. A., 2001, *ApJ*, **554**, 1290
Hjellming R. M., Rupen M. P., 1995, *Nature*, **375**, 464
Homan J., et al., 2020, *ApJ*, **891**, L29
Ingram A. R., Motta S. E., 2019, *New Astron. Rev.*, **85**, 101524
Ingram A., Done C., Fragile P. C., 2009, *MNRAS*, **397**, L101
Ingram A., van der Klis M., Middleton M., Done C., Altamirano D., Heil L., Uttley P., Axelsson M., 2016, *MNRAS*, **461**, 1967
Karpouzas K., Méndez M., Ribeiro E. M., Altamirano D., Blaes O., García F., 2020, *MNRAS*, **492**, 1399
Krawczynski H., et al., 2022, arXiv e-prints, p. arXiv:2206.09972
Kubota A., Tanaka Y., Makishima K., Ueda Y., Dotani T., Inoue H., Yamaoka K., 1998, *PASJ*, **50**, 667
Kumar N., Misra R., 2014, *MNRAS*, **445**, 2818
Kylafis N. D., Reig P., 2018, *A&A*, **614**, L5
Kylafis N. D., Reig P., Papadakis I., 2020, *A&A*, **640**, L16

- Lasota J.-P., 2001, *New Astron. Rev.*, **45**, 449
- Lee H. C., Miller G. S., 1998, *MNRAS*, **299**, 479
- Lee H. C., Misra R., Taam R. E., 2001, *ApJ*, **549**, L229
- Makishima K., Maejima Y., Mitsuda K., Bradt H. V., Remillard R. A., Tuohy I. R., Hoshi R., Nakagawa M., 1986, *ApJ*, **308**, 635
- Mastichiadis A., Petropoulou M., Kylafis N. D., 2022, *A&A*, **662**, A118
- Méndez M., Karpouzas K., García F., Zhang L., Zhang Y., Belloni T. M., Altamirano D., 2022, *Nature Astronomy*, **6**, 577
- Mitsuda K., et al., 1984, *PASJ*, **36**, 741
- Miyamoto S., Kitamoto S., Mitsuda K., Dotani T., 1988, *Nature*, **336**, 450
- Miyamoto S., Kimura K., Kitamoto S., Dotani T., Ebisawa K., 1991, *ApJ*, **383**, 784
- Molteni D., Sponholz H., Chakrabarti S. K., 1996, *ApJ*, **457**, 805
- Motta S., Homan J., Muñoz-Darias T., Casella P., Belloni T. M., Hiemstra B., Méndez M., 2012, *MNRAS*, **427**, 595
- Motta S. E., Belloni T. M., Stella L., Muñoz-Darias T., Fender R., 2014, *MNRAS*, **437**, 2554
- Motta S. E., Casella P., Henze M., Muñoz-Darias T., Sanna A., Fender R., Belloni T., 2015, *MNRAS*, **447**, 2059
- Muñoz-Darias T., Motta S., Belloni T. M., 2011, *MNRAS*, **410**, 679
- Nathan E., et al., 2022, *MNRAS*, **511**, 255
- Nobili L., Turolla R., Zampieri L., Belloni T., 2000, *ApJ*, **538**, L137
- Nowak M. A., 2000, *MNRAS*, **318**, 361
- Peirano V., Méndez M., 2022, *MNRAS*, **513**, 2804
- Peirano V., Méndez M., García F., Belloni T., 2023, *MNRAS*, **519**, 1336
- Pottschmidt K., et al., 2003, *A&A*, **407**, 1039
- Psaltis D., Belloni T., van der Klis M., 1999, *ApJ*, **520**, 262
- Rawat D., et al., 2023, *MNRAS*, **520**, 113
- Reig P., Kylafis N. D., 2019, *A&A*, **625**, A90
- Reis R. C., Fabian A. C., Ross R. R., Miller J. M., 2009, *MNRAS*, **395**, 1257
- Remillard R. A., Sobczak G. J., Munro M. P., McClintock J. E., 2002, *ApJ*, **564**, 962
- Rink K., Caiazzo I., Heyl J., 2022, *MNRAS*, **517**, 1389
- Russell T. D., et al., 2019, *ApJ*, **883**, 198
- Schnittman J. D., Homan J., Miller J. M., 2006, *ApJ*, **642**, 420
- Shafee R., McClintock J. E., Narayan R., Davis S. W., Li L.-X., Remillard R. A., 2006, *ApJ*, **636**, L113
- Shakura N. I., Sunyaev R. A., 1973, *A&A*, **500**, 33
- Shaposhnikov N., 2012, *ApJ*, **752**, L25
- Sobolewska M. A., Zycki P. T., 2006, *MNRAS*, **370**, 405
- Stella L., Vietri M., 1998, *ApJ*, **492**, L59
- Stevens A. L., Uttley P., 2016, *MNRAS*, **460**, 2796
- Stuchlík Z., Kološ M., 2016, *A&A*, **586**, A130
- Sunyaev R. A., Truemper J., 1979, *Nature*, **279**, 506
- Tagger M., Pellat R., 1999, *A&A*, **349**, 1003
- Uttley P., Klein-Wolt M., 2015, *MNRAS*, **451**, 475
- Uttley P., Wilkinson T., Cassatella P., Wilms J., Pottschmidt K., Hanke M., Böck M., 2011, *MNRAS*, **414**, L60
- Uttley P., Cackett E. M., Fabian A. C., Kara E., Wilkins D. R., 2014, *A&ARv*, **22**, 72
- Verner D. A., Ferland G. J., Korista K. T., Yakovlev D. G., 1996, *ApJ*, **465**, 487
- Wagoner R. V., Silbergleit A. S., Ortega-Rodríguez M., 2001, *ApJ*, **559**, L25
- Wilms J., Allen A., McCray R., 2000, *ApJ*, **542**, 914
- Zdziarski A. A., Johnson W. N., Magdziarz P., 1996, *MNRAS*, **283**, 193
- Zhang Y., et al., 2022, *MNRAS*, **512**, 2686
- Zhang Y., et al., 2023, *MNRAS*, **520**, 113
- Zycki P. T., Done C., Smith D. A., 1999, *MNRAS*, **309**, 561
- van den Eijnden J., Ingram A., Uttley P., Motta S. E., Belloni T. M., Gardenier D. W., 2017, *MNRAS*, **464**, 2643
- van der Klis M., 1989, *ARA&A*, **27**, 517

This paper has been typeset from a \LaTeX file prepared by the author.